RSC Advances

PAPER

View Article Online
View Journal | View Issue

Cite this: *RSC Adv.*, 2022, **12**, 21374

Electrochemical performance of $CoSe_2$ with mixed phases decorated with N-doped rGO in potassium-ion batteries†

Hui Zheng,‡[b] Han-Shu Xu, ‡*[ab] Jiaping Hu,[b] Huimin Liu,[b] Lianwei Wei,[b] Shusheng Wu,[b] Jin Li,[b] Yuhu Huang[b] and Kaibin Tang *[ab]

Received 11th June 2022
Accepted 19th July 2022

DOI: 10.1039/d2ra03608h

rsc.li/rsc-advances

Potassium-ion batteries (PIBs) have received much attention as next-generation energy storage systems because of their abundance, low cost, and slightly lower standard redox potential than lithium-ion batteries (LIBs). Nevertheless, they still face great challenges in the design of the best electrode materials for applications. Herein, we have successfully synthesized nano-sized $CoSe_2$ encapsulated by N-doped reduced graphene oxide (denoted as $CoSe_2$@N-rGO) by a direct one-step hydrothermal method, including both orthorhombic and cubic $CoSe_2$ phases. The $CoSe_2$@N-rGO anodes exhibit a high reversible capacity of 599.3 mA h g^{-1} at 0.05 A g^{-1} in the initial cycle, and in particular, they also exhibit a cycling stability of 421 mA h g^{-1} after 100 cycles at 0.2 A g^{-1}. Density functional theory (DFT) calculations show that $CoSe_2$ with N-doped carbon can greatly accelerate electron transfer and enhance the rate performance. In addition, the intrinsic causes of the higher electrochemical performance of orthorhombic $CoSe_2$ than that of cubic $CoSe_2$ are also discussed.

1. Introduction

LIBs are widely used in the field of energy storage due to their high energy density and excellent power density.[1–3] Meanwhile, the limited and unevenly distributed lithium resources not only make LIBs expensive, but also severely limits the large-scale application of LIBs.[4] Consequently, it is urgent to explore new and low-cost energy storage devices. The working principles of PIBs and LIBs are similar, and the reserves of potassium resources are relatively rich, the cost is low, and the redox potential of PIBs is very close to that of lithium (K^+/K: −2.93 V; Li^+/Li: −3.04 V).[5,6] Therefore, PIBs are one of the ideal substitutes for LIBs, especially in large-scale energy storage applications. Although theoretically feasible, there are still some difficulties in the application of PIBs.[7–9] On the one hand, the diffusion process of K^+ in the bulk phase of traditional electrode materials is difficult due to its large ion radius, and on the other hand, the large volume change associated with the K^+ insertion/extraction of the electrode materials significantly reduces the capacity of the battery.[10–12] In order to solve these technical problems, it is necessary to carry out reasonable structural and morphological design of key electrode materials for PIBs.

Carbon-based materials usually show the better chemical stability, and can act as an elastic buffer carrier to increase the stability of electrode materials during circulation.[13,14] The advantages of rich pore structure and high conductivity make it have excellent performance as protective load material and electrode material, so it is an important anode material of PIBs. Among them, hard carbon and N-doped carbon has more active sites and larger discharge capacity, which has attracted the attention of researchers.[13,15,16] However, the current carbon electrode has a lower theoretical capacity of 372 mA h g^{-1}, and the lower working potential will accelerate the formation of dendritic Li/Na/K at a high rate, which will greatly weaken the energy density of the battery and reduce the safety of use.[13] Therefore, the development of PIBs anode composites with large capacity and excellent cycling performance is the key to overcome these shortcomings and meet the needs of large-scale energy storage equipment.

Compared with transition metal sulfides, transition metal selenium compounds not only have higher electrical conductivity, but also weaker ionic bonds and larger spacing between metal ions and selenium ions can significantly improve ionic diffusion kinetics and electrochemical performance.[17,18] The disadvantage of transition metal selenides is that large particle agglomeration and severe volume expansion often occur in alloying or conversion reactions, resulting in rapid capacity loss and reduced cycle life.[19] After a long period of exploration, it has been found that combination of carbon materials and

[a]*Hefei National Research Center for Physical Sciences at the Microscale, University of Science and Technology of China, Hefei, 230026, People's Republic of China. E-mail: xhs@ustc.edu.cn; kbtang@ustc.edu.cn*

[b]*Department of Chemistry, University of Science and Technology of China, Hefei, 230026, People's Republic of China*

† Electronic supplementary information (ESI) available. See https://doi.org/10.1039/d2ra03608h

‡ Hui Zheng and Han-Shu Xu make the same contribution to this work.

transition metal selenides is an effective method to eliminate the disadvantages when they exist alone through technical means such as nano crystallization, nanostructure engineering and carbon coating.[6,20] The volume changes buffered by the construction of metal-carbon and selenium-carbon chemical bonds, improving the electrochemical performance.[6,21]

After the development in recent years, transition metal selenides with different nano-morphologies, such as $CoSe_2$, Ni_3Se_4, $MoSe_2$, *etc.*, are often used as anode materials for PIBs.[22,23] These transition metal selenides coated with different morphologies and types of carbon show good cycle stability and large residual capacitance in PIBs. For example, Xu *et al.* prepared $CoSe_2$–$MoSe_2$/rGO composite electrode materials, and the formation of chemical bonds between the two significantly improved the charge transfer in the electrochemical cycle.[23] Among these transition metal selenides for PIBs and sodium-ion batteries (SIBs), $CoSe_2$ is special, because according to the current reports, no matter how carbon is used for modification, the electrochemical cycle performance of $CoSe_2$ belonging to the orthorhombic system is always better than that of the cubic system.[24–30] In addition, the actual reaction processes from $CoSe_2$ with orthorhombic structure to Co and K_2Se have been theoretically given, which is significantly different from LIBs and SIBs.[19,20,24,31–33] To further understand the behavior of $CoSe_2$ with different crystal systems in PIBs, more experiments and theoretical calculations are necessary.

In this study, nano-sized $CoSe_2$ was decorated by N-doped reduced graphene oxide (denoted as $CoSe_2$@N-rGO) through a direct one-step hydrothermal synthesis, which contains both orthorhombic and cubic phase. The electrochemical capability of the $CoSe_2$@N-rGO compound was evaluated as anode materials for PIBs. Particularly, the $CoSe_2$@N-rGO nanoparticles delivered a high reversible capacity of 599.3 mA h g^{-1} at 0.05 A g^{-1} in the first circle, and exhibited a reversible capacity of 421 mA h g^{-1} at 0.2 A g^{-1} after 100 cycles. The density of states (DOS) of different situations and the effect of carbon coating on the DOS was obtained by the DFT calculations, and the intrinsic physics of the excellent electrochemical performance of the orthorhombic $CoSe_2$@N-rGO was further discussed, which is helpful to deepen understanding of composites in the electrochemical reaction.

2. Results

The synthesis strategy for $CoSe_2$ encapsulated by N-doped carbon with a sandwich-like structure in a whole is

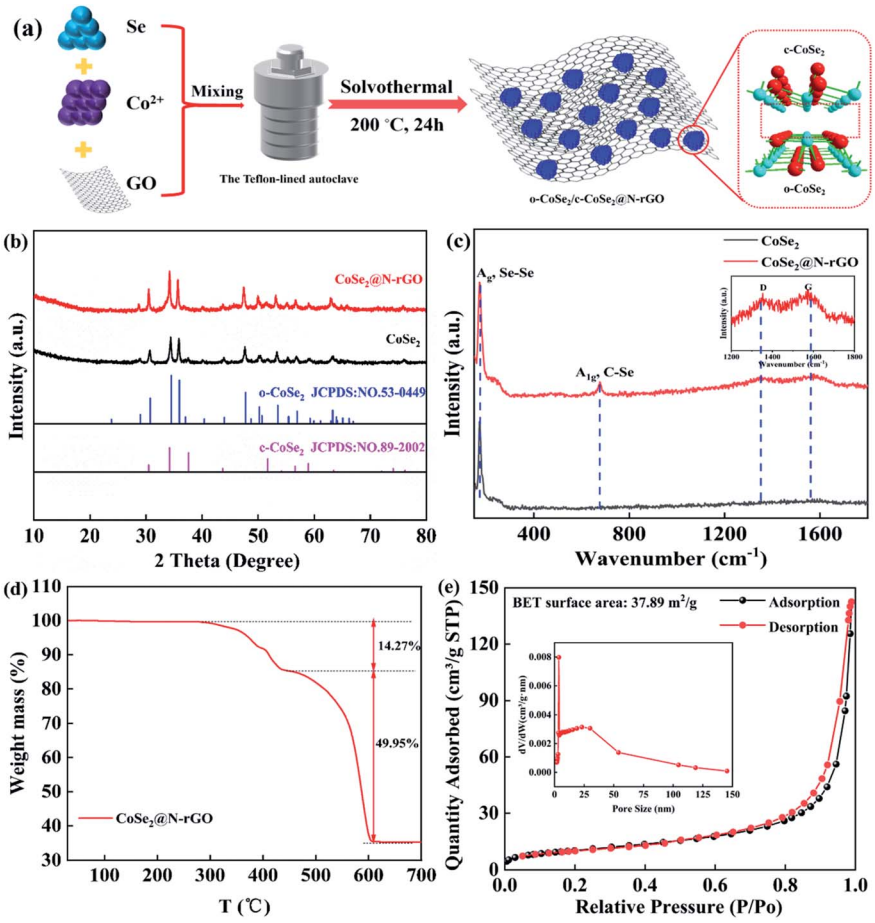

Fig. 1 Characterization of $CoSe_2$@N-rGO nanocomposites obtained *via* one-step solvothermal method. (a) Schematic representation of the synthesis process, (b) XRD patterns, (c) Raman spectra, (d) TGA curve, and (e) N_2 adsorption/desorption profile (inset: corresponding pore size distribution). Here, *o*-$CoSe_2$ represent orthorhombic $CoSe_2$ and c-$CoSe_2$ represent cubic $CoSe_2$.

schematically described in Fig. 1(a). The XRD patterns confirm that $CoSe_2$ contains two phases (Fig. 1(b)), the main phase has an orthorhombic structure (JCPDS no. 53-0449), and the other small amount of phase belongs to cubic phase (JCPDS no. 89-2002). Importantly, this further indicates that we have successfully synthesized $CoSe_2$ containing a small amount of cubic phase, which could form a heterojunction with orthorhombic $CoSe_2$. Moreover, there was no carbon peak observed in XRD patterns, which implies that the low amorphous carbon content and great crystallinity of $CoSe_2$. To gain a better understanding of amorphous carbon, samples $CoSe_2$ and $CoSe_2$@N-rGO were evaluated by Raman spectroscopy (Fig. 1(c)). Compared with $CoSe_2$, there are double distinct peaks at 1337.73 and 1598.55 cm^{-1} for $CoSe_2$@N-rGO, which correspond to the sp^3-hybridization vibration of disordered or defective bands (D-band) and sp^2-stretching of graphitic bands (G-band) of amorphous carbon, respectively. From the inset in Fig. 1(c), it is clearly visible from the intensity of D-band on $CoSe_2$@N-rGO is comparable to that of the G-band (the ratio $I_D/I_G \approx 1.15$), revealing that the amorphous coated carbon has more defects and disorder.[13,34,35] Meanwhile, the existence of these defects and disorder can also form a strong interaction with $CoSe_2$@N-rGO during electrochemical cycling reactions. In addition, the peak at 173.7 cm^{-1} (A_g) is assigned to the Se–Se in $CoSe_2$@N-rGO, while a tiny peak associated with C–Se bond appears at 677.2 cm^{-1} (A_{1g}).[36–38] The presence of C–Se bond between $CoSe_2$ and N-rGO is not simple physical contact but it is a kind of chemical connection through C–Se bond.

To further understand the thermal stability of $CoSe_2$@N-rGO and confirm the relative contents of $CoSe_2$ and carbon of $CoSe_2$@N-rGO composites, we performed a TG analysis of the as-synthesized samples $CoSe_2$@N-rGO. Fig. 1(d) shows the representative TG curve on heating up from room temperature to 700 °C in hot air at a rate of 10 °C min^{-1}. Firstly, the weight of $CoSe_2$@N-rGO is almost unchanged below 300 °C, which indicates that it has good thermal stability. When the temperature surpasses 300 °C, the weight reduction is attributed to the oxidative decomposition of the N-rGO to CO_2 and NO_2. However, when the temperature above 410 °C, the rapid weight decrease should be caused by the oxidation of $CoSe_2$ to Co_3O_4.[38,39] Corresponding to the TG curve, the content of organic coating in $CoSe_2$@N-rGO compounds accounts for about 14.27%. Fig. 1(e) and S1† show the isothermal nitrogen adsorption/desorption and nanopore size distribution curves of $CoSe_2$@N-rGO and $CoSe_2$, respectively. After comparison, it is found that the $CoSe_2$ coated with N-doped carbon exhibits higher nitrogen adsorption/desorption value in a whole, and the curve has a smaller hysteresis behavior. The insets in Fig. 1(e) and S1† illustrate that the peaks of pore size before and after N-doped carbon coating are 18 nm and 25 nm, respectively. The introduction of N-rGO can accelerate ion diffusion, which is beneficial to the electrode reaction.[40,41] Furthermore, a sharp peak at around 3.5 nm can also be clearly seen in the inset of Fig. 1(e), which corresponds to the averaged nanopore size of N-doped carbon.

Chemical composition and chemical bonding situation of $CoSe_2$@N-rGO composites can be determined by XPS analysis, as seen in Fig. 2(a)–(d). High-resolution spectra confirmed the existence of Co, Se, C and N elements in the $CoSe_2$@N-rGO (Fig. S2†). Fig. 2(a) shows that there are six peaks on the Co 2p spectrum, which can be well fitted by Co^{3+}, Co^{2+} and two other satellite peaks. Two broad peaks located at 797.2 eV and 781.3 eV correspond to Co^{2+} $2p_{1/2}$ and Co^{2+} $2p_{3/2}$, respectively, while the peaks at 785.4 eV and 802.8 eV stem from the corresponding satellite peaks of Co^{2+}. The Co–O bond of Co_2O_3 (Co^{3+}) due to the surface oxidization of $CoSe_2$, resulting in peaks at 779.1 eV and 794.1 eV.[37,42,43] The two peaks at 54.8 eV and 55.6 eV in Fig. 2(b) can be assigned to Se $3d_{5/2}$ and Se $3d_{3/2}$,

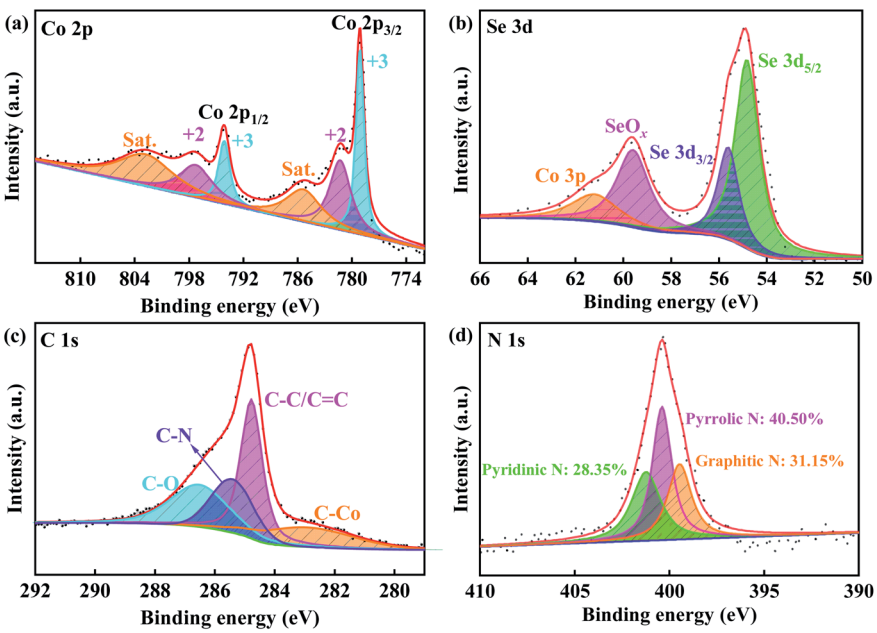

Fig. 2 XPS spectra of $CoSe_2$@N-rGO compounds: (a) Co 2p, (b) Se 3d, (c) C 1s, and (d) N 1s spectrum.

respectively. The peaks located at 59.6 eV is corresponding to Se–O bond formed by the inevitable surface oxidation of the transition metal selenides during the test.[22,23,42] The broad peak at around 61.2 eV is assigned to the Co 3p orbital.[41,44]

Fig. 2(c) shows the spectrum of C 1s, three peaks located at 284.7 eV, 285.1 eV and 286.3 eV should belong to C–C/C=C, C–N, and C–O bonds, respectively.[45] Importantly, the C–Co bond can also be observed at 282.4 eV, which indicates that there is not a simple physical contact but a strong interaction between the $CoSe_2$ and the carbon layer, thus ensuring the stability and robustness of the $CoSe_2$@N-rGO composites.[46] Furthermore, the carbon is nitrogen-doped, and the N 1s XPS spectrum of nitrogen in the carbon layer is shown in Fig. 2(d). The three peaks at 399.5 eV, 400.4 eV and 401.2 eV are corresponding to graphitic N, pyrrolic N and pyridinic N, respectively. By calculation, the content of each type of nitrogen (graphitic, pyrrolic, and pyridinic) are 31.15%, 40.50% and 28.35%, respectively. The abundant N-doping provides more exogenous defects and

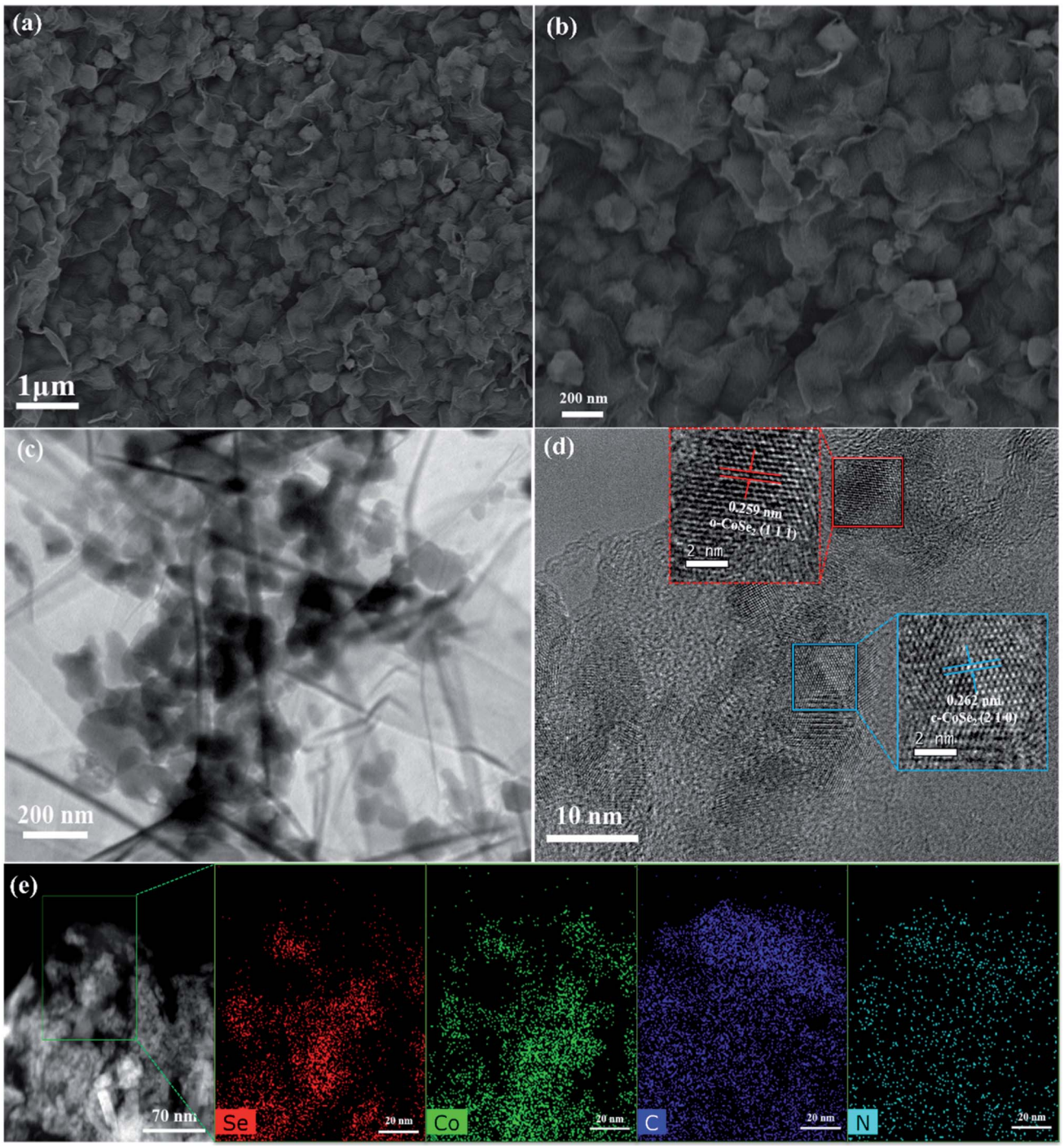

Fig. 3 Morphology and microstructure characterizations of the $CoSe_2$@N-rGO: (a and b) SEM, (c) TEM, (d) HRTEM, and (e) EDS mappings of the Se, Co, C and N elements.

active centers to improve electron/ion transport in electrochemical reactions, thereby further improving conductivity and increasing reversible capacity.[38,47,48]

In order to directly observe the coating of N-doped reduced graphene oxide on $CoSe_2$ nanoparticles, SEM was used for characterization. Fig. S3(a)† shows that the overall shape of uncoated $CoSe_2$ is not uniform, some are spherical, some are flake, and some are rod-like structures, which also reflects $CoSe_2$ synthesized by one-step method is a mixed phase with multiple structures. The nano-sized $CoSe_2$ results of TEM in Fig. S3(b)† also further verify the results of SEM. It is shown that the $CoSe_2$ nanoparticles are evenly distributed in $CoSe_2$@N-rGO, the SEM images with a large-scale range in Fig. 3(a), signifying that one-step synthesis method we used can also effectively avoid the aggregation of $CoSe_2$ nanoparticles. From Fig. 3(b), the N-doped carbon tightly wraps $CoSe_2$, which enables the chemical structure stability of $CoSe_2$ to be effectively improved during electrochemical cycling. In addition, the size of $CoSe_2$@N-rGO nanoparticles is about 150–200 nm. The TEM and HRTEM images in Fig. 3(c) and S3(d)† further elucidated that the $CoSe_2$@N-rGO with uniform size are homogenously well-encapsulated in N-doped carbon frame network rather than exposed to the surface. Fig. 3(d) shows the HRTEM image of $CoSe_2$@N-rGO, the d = 0.262 nm is assigned to the (210) crystal planes of $CoSe_2$ with cubic crystal structure, whereas the (111) plane of $CoSe_2$ with orthorhombic crystal structure comes down to the interplanar distance of 0.259 nm. In fact, these two different crystals of $CoSe_2$ can be effectively constructed into heterointerface, which can improve the electrochemical reaction kinetics by promoting the transport of alkali metal ions. Additionally, Fig. 3(e) exhibit the evenly distribution of Co, Se, C and N elements in the chosen $CoSe_2$@N-rGO composites. Moreover, from the C, N, Co, and Se peak intensity line traces in the EDX spectra of $CoSe_2$@N-rGO composites (shown in Fig. S3(e)†), it is concluded that C, N, Co, and Se have been almost homogeneously distributed throughout the samples. From the EDS mapping in Fig. S3(c),† it also can be seen that the pristine $CoSe_2$ contains a very small amount of N and C, which is mainly due to the inevitable introduction of C and N from ethylenediamine during the reaction. The prominent Cu element peaks in EDX originate from the copper-containing sample holder.

To further understand the mechanism of potassium storage, CR2032 coin-type cells were assembled at room temperature to systematically study the electrochemical performance of the $CoSe_2$@N-rGO. The CV curves of Fig. 4(a) shows that during the first discharge (cathodic) scan, a strong reduction peak locate at 0.71 V and at 0.82 V has a small kink, which corresponds to the formation of Co_3KSe_4 by inserting K^+ into the $CoSe_2$ layer, accompanied by the formation of solid electrolyte interface (SEI) layer on the electrode and electrolyte interface. Meanwhile, due to the reduction of Co_3KSe_4 to Co and K_2Se by K^+, another small reduction peak can be observed at 0.35 V. In contrast, the oxidation peaks in 1.12 V and 1.67 V are consistent with the sequential reverse conversion reaction from K_2Se and Co to Co_3KSe_4 in the first charging (anodic) cycle.[49] A stronger oxidation peak appears at 2.26 V and a minor peak lies in 2.1 V, which are attributed to the de-intercalation of K^+ from Co_3KSe_4 to $CoSe_2$. In the following CV scans, the peak positions of the reduction peaks shift to higher voltages, while the oxidation peaks are almost unchanged, indicating that the polarization of $CoSe_2$@N-rGO electrode is small.[43,50] In fact, the apparent difference between the first scan and the subsequent scan is mainly due to the formation of SEI.[51,52]

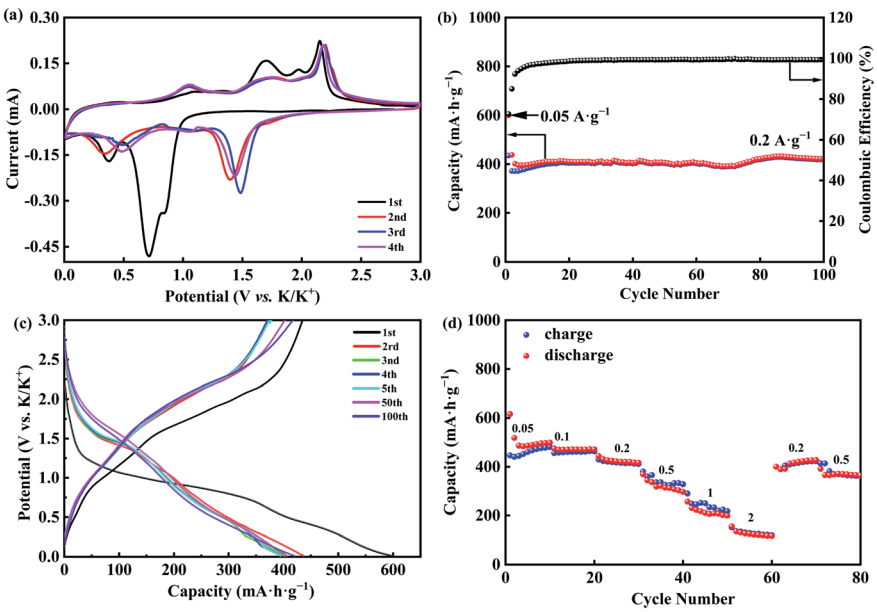

Fig. 4 Electrochemical property in PIBs of $CoSe_2$@N-rGO composite. (a) The CV curves within a voltage window of 0.01–3.0 V at a scan rate of 0.1 mV s^{-1} during the first four cycles. (b) Galvanostatic charge/discharge capacity and coulombic efficiency at 0.2 A g^{-1} except for the initial cycle at 0.05 A g^{-1}. (c) Charge/discharge curves at 0.05 A g^{-1} for the first cycle, and 0.2 A g^{-1} for the 2nd, 3rd, 4th, 5th, 50th, and 100th cycles. (d) Rate performance at various current densities.

It is well known that the repeated insertion/extraction of large K^+ often leads to structural failure, so that cycle performance is vital to rechargeable PIBs. From Fig. 4(b), the $CoSe_2$@N-rGO anode material shows the capacity of 599.3 mA h g^{-1} at 0.05 A g^{-1} during the initial circle, and keeps 421 mA h g^{-1} at 0.2 A g^{-1} after 100 cycles, which prove $CoSe_2$@N-rGO present better cycling stability. In order to highlight the significant function of N-doped carbon coating, we also tried to conduct electrochemical experiments with uncoated $CoSe_2$, and the results show that the battery capacity decays rapidly with the increase of the number of cycles (shown in Fig. S4†). The charge/discharge profiles in Fig. 4(c) are consistent with the CV profiles. The $CoSe_2$@N-rGO anode provides a large capacity of 599.3 mA h g^{-1} with a low initial coulombic efficiency of 72.6% during the initial cycle. In the following cycles, the reversible discharge curves have good coincidence, denoting that the electrochemistry maintains the cycle stability. In should be noted that the capacity decreases and coulombic efficiency increases during first three cycles due to formation of stable SEI film.[51] Moreover, the discharge curve exhibits a slightly sloping step at around 1.5 V and about 2.0 V on the charge curve, which agree well with the 1.48 V reduction peak and the 2.1 V oxidation peak on the CV curve, respectively. Interestingly, with the increase of the number of cycles, the possible reason for the increase of capacity is the electrochemical reconstruction or electrochemical activation process during the reaction, which can provide plentiful sites for K^+-storage.[53]

Fig. 4(d) demonstrates the rate performance of $CoSe_2$@N-rGO composites at several current densities. The $CoSe_2$@N-rGO reversible capacities obtained are 498.5, 470.9, 415.8, 296.8 and 199.3 mA h g^{-1} at the different current density of 0.05 A g^{-1}, 0.1, 0.2, 0.5 and 1 A g^{-1}. Interestingly, $CoSe_2$@N-rGO has an excellent reversible capacity of 116.7 mA h g^{-1} when the current density is even up to 2 A g^{-1}. Importantly, due to the rearrangement of structure in the process of reaction activation and the production of more active sites when K^+ insertion/extraction during the reaction, the capacity could recover to close to the previous values of 427.1 and 364.1 mA h g^{-1} after 60 cycles whether the current density returns to 0.2 or 0.5 A g^{-1}, indicating fine reliability and rate performance.[54] For the long-term cycling performance by the extended charge and discharge experiments, the initial discharge capacity shown in Fig. S5(a)† is about 624.9 mA h g^{-1} at 0.05 A g^{-1} with initial coulombic efficiency of 72.2%, which is relatively close to the low current 0.05 A g^{-1} as in Fig. 4(d). As shown in Fig. S5(a) and (b),† the capacity begins to decay after about 200 cycles, while the reversible capacity of $CoSe_2$@N-rGO is only 174.7 mA h g^{-1} beyond 400 cycles at 1 A g^{-1}. Therefore, it can be speculated that the structural distortion of $CoSe_2$ leads to the decreased long-term cycling performance during the long-term cycling of potassiation/de-potassiation.

Fig. 5(a) plots the CV curves at various scan rates ranging from 0.2 to 1.0 mV s^{-1}. Overall, the CV loops exhibit similar shapes at different scanning rates, indicating that there is the identical electrochemical process at the scanning rate. Based on the Bruce Dunn's theory,[55,56] by the following equations, the relationship between the peak current (i) and scan rate (v) can be expressed:

$$i = av^b \quad (1)$$

$$\log(i) = \log(a) + b\log(v) \quad (2)$$

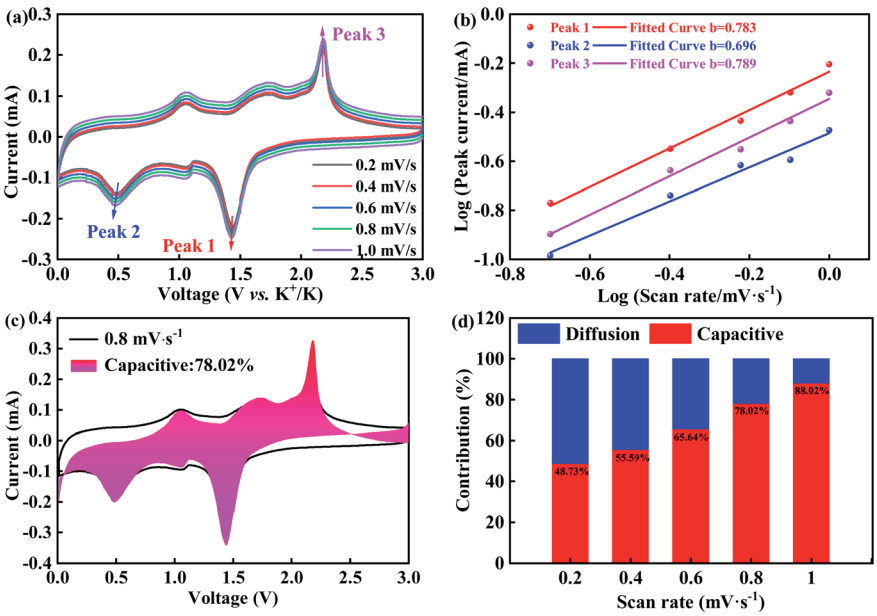

Fig. 5 Electrochemical kinetics analysis of $CoSe_2$@N-rGO composites. (a) CV profiles at different scan rates within 0.01–3.0 V. (b) Plots of log(i) *vs.* log(v) for three peaks in the CV curves. (c) Pseudocapacitive contribution was calculated as 78.02% and displayed by the shaded region at 0.8 mV s^{-1}. (d) Bar graph displaying the calculated contributed ration of the capacitive and diffusion-controlled capacity to the overall capacity at distinct scan rates.

where the b value is the slope of the linear relationship between $\log(v)$ and $\log(i)$, and a and b are all fitting parameters. The electrochemical process is dominated by diffusion-controlled behavior when the value of b is near to 0.5, while in case the value of b is approximately equal to 1, the surface-controlled reaction is dominate.[57] That is, the b value is usually used to interpret the potassium storage behaviors (b = 0.5: K-ion intercalation; b = 1: capacitive-controlled process). The plots ($\log(v)$ *vs.* $\log(i)$) are shown for three peaks in the CV curves, as shown in Fig. 5(b). The b value of 0.783, 0.696 and 0.789 belong to the peak 1, 2 and 3, respectively, recommending that the kinetic process of the electrode is mainly a capacitive-controlled process.

To investigate their contributions, the following eqn (3) is used,

$$i = k_1 v + k_2 v^{1/2} \quad (3)$$

where, $k_1 v$ represent the capacitive-controlled contributions, and $k_2 v^{1/2}$ diffusion-controlled contributions, respectively.[56] Fig. 5(c) illustrates that nearly 78.02% (shaded region) of the overall charge storage stems from capacitive contribution at 0.8 mV s^{-1}, implying that the capacitive contribution is leading at 0.8 mV s^{-1}. Using the same method, the capacitive contribution is reckoned to be 48.73% at 0.2 mV s^{-1}, 55.59% at 0.4 mV s^{-1}, 65.64% at 0.6 mV s^{-1} and 88.02% at 1.0 mV s^{-1}, respectively, which gradually increases with the increase of scanning rate, as shown in Fig. 5(d). On account of our experimental results, it is shown that the charge storage mechanism of $CoSe_2$@N-rGO includes both K-ion intercalation and capacitive contributions, but the capacitance contribution plays a leading role, especially at high scan rate. This means that the unique encapsulation structure and the synergistic effect of ultrahigh conductivity in the N-doped carbon skeleton make the $CoSe_2$@N-rGO with larger specific surface area exhibit excellent rate performance.

3. Discussion

In this work, we synthesized $CoSe_2$ with two different crystal structures by one-step method, in which the orthorhombic one is the dominant phase. In $CoSe_2$ with mixed phase, the electrochemical cycling process consists of three independent processes, one for orthorhombic system, one for cubic system, and the last is for heterojunction formed by orthorhombic and cubic system, among which the first is the main one. Table S1 and S2† show that as the anode materials of PIBs and SIBs, $CoSe_2$ with orthogonal phase often exhibits better cycling performance than that with cubic phase, although both have experienced different forms of coating. Although some previous experimental works have given the reaction equations during electrochemical cycling, it is inaccurate to simply replace Li/Na with K in the equation of LIBs and SIBs due to the larger radius of K^+. The process of K^+ intercalation into $CoSe_2$ with orthogonal phase has been carefully studied by the first-principles calculations, and the reaction equation is as follows:[58]

$$CoSe_2 + 4/3K^+ + 4/3e^- \rightarrow 1/3Co_3Se_4 + 2/3K_2Se \quad (4)$$

$$Co_3Se_4 + K^+ + e^- \rightarrow Co_3KSe_4 \quad (5)$$

$$Co_3KSe_4 + K^+ + e^- \rightarrow 3CoSe + K_2Se \quad (6)$$

$$CoSe + 2K^+ + 2e^- \rightarrow Co + K_2Se \quad (7)$$

In charging process, the reaction equation can be summarized into the following steps:

$$4K_2Se + 3Co \rightarrow Co_3KSe_4 + 7K^+ + 7e^- \quad (8)$$

$$Co_3KSe_4 + 2K_2Se \rightarrow 3CoSe_2 + 5K^+ + 5e^- \quad (9)$$

As shown in Fig. 4(a), our CV results are basically consistent with the experimental results of Yu *et al.*, eqn (4)–(7) can also well describe our discharge processes.[58] In addition, compared with Yu's results, there is no additional peak on our CV curve, so it can be inferred that the above reaction eqn (4)–(9) are also followed for the $CoSe_2$ with cubic phase during electrochemical cycling.[58]

Now we focus on the influence of carbon coating for the electrochemical performance of $CoSe_2$@N-rGO anode material. By means of the DFT calculations, we obtained the DOS profiles of $CoSe_2$ with orthorhombic phases, cubic phases, and the heterojunction constructed by these two structures, respectively. The detailed lattice model used in the DFT calculations is constructed in Fig. S7.† Fig. 6(a) exhibit that the DFT results reveal the metallic behavior of the orthorhombic $CoSe_2$, in which the DOS resides across the Fermi level, giving promising signs for the high conductivity of nanoparticles. Importantly, the electronic configuration of orthorhombic $CoSe_2$ is $t_{2g}^6 e_g^1$, which means that the effective magnetic moment of its ground state is not zero, and therefore, the DOS is asymmetric.[58] Compared with $CoSe_2$, Fig. 6(d) shows that the DOS of $CoSe_2$@N-rGO changes greatly. Significantly, the overall DOS of $CoSe_2$@N-rGO increases several times, and the forbidden band between 3–4 V and −8 to −12 V disappears, which fully indicates the conductivity will be batter after coating. Furthermore, the electrochemical impedance spectroscopy (EIS) of Fig. S6† also verifies the significant decrease of the overall resistivity after carbon coating. After comparing Fig. 4(b) and S4,† it can be found the cycle stability of $CoSe_2$@N-rGO is much higher than that of $CoSe_2$. However, the capacity of the first 30 cycles is not as good as $CoSe_2$, indicating that the carbon coating mainly plays a part in maintaining the structure of $CoSe_2$. For $CoSe_2$ with cubic structure, the DOS is shown in Fig. 6(b). The profiles show that the p-orbital of Se and the d-orbital of Co through the Fermi level, indicating that the cubic $CoSe_2$ is metallic. Moreover, its positive (spin up) and negative (spin down) total DOS is symmetrical, which also implies that the Co ions exhibit paramagnetism. Our DFT results are consistent with the previous measurements of transport and paramagnetic behavior.[59] The DOS of cubic $CoSe_2$ after carbon coating is shown in Fig. 6(e), which shows a similar result to the Fig. 6(d), namely, the disappearance of the bandgap in a larger energy range.

Theoretically, the capacitance of $CoSe_2$ is certain and independent of the structure. In some transition metal compounds,

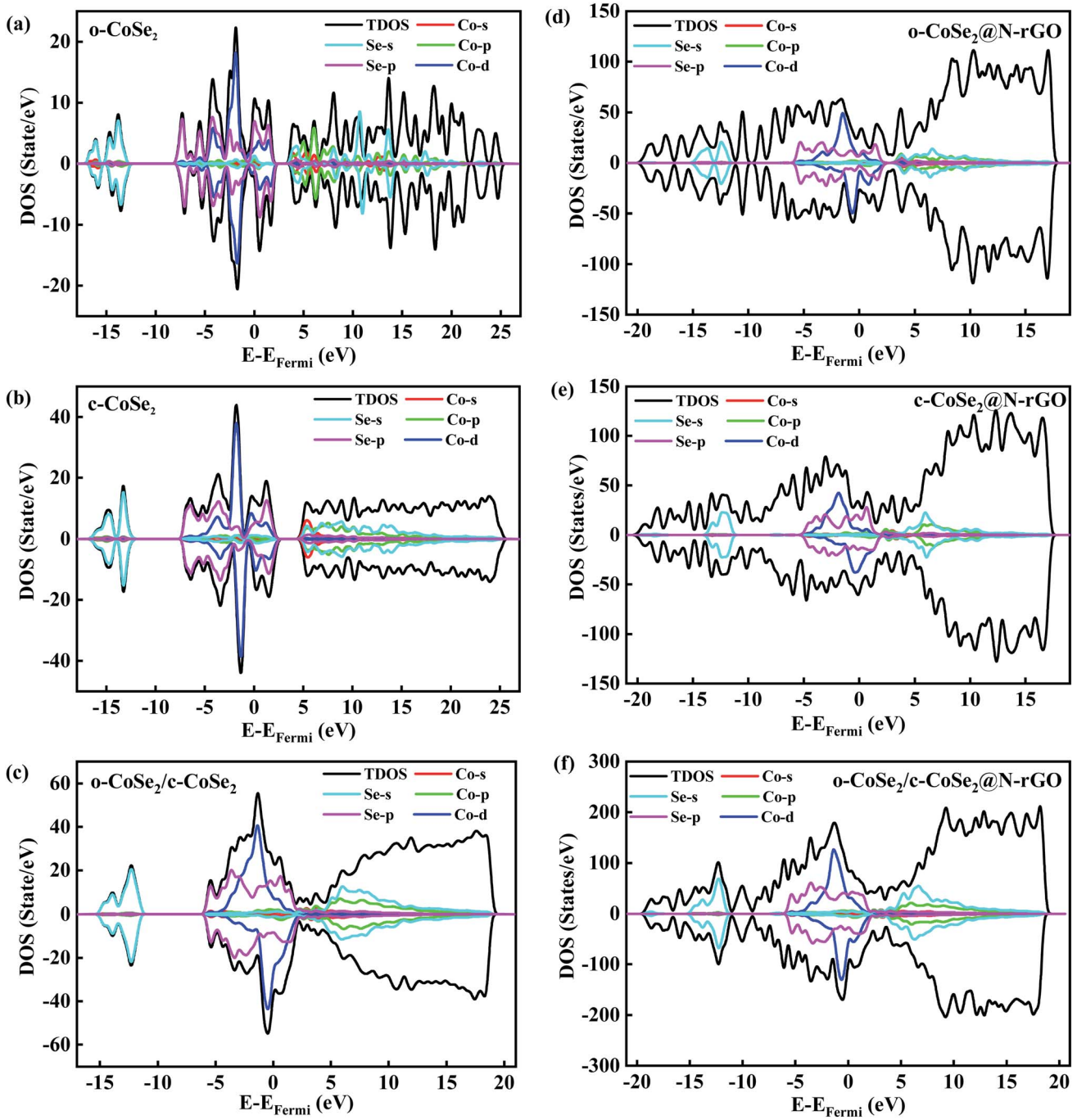

Fig. 6 DOS based on DFT calculations of the (a) *o*-$CoSe_2$, (b) c-$CoSe_2$ and (c) *o*-$CoSe_2$/c-$CoSe_2$, (d) *o*-$CoSe_2$@N-rGO, (e) c-$CoSe_2$@N-rGO and (f) *o*-$CoSe_2$/c-$CoSe_2$@N-rGO. Here, *o*-$CoSe_2$ represent orthorhombic $CoSe_2$ and c-$CoSe_2$ represent cubic $CoSe_2$.

such as Fe_3O_4, CoO, NiO, FeF_2 and Fe_2N, the extra capacitance is mainly derived from the spin-polarized capacitance on the surface of the transition metal nanoparticle, and the high DOS of 3d electrons at the Fermi surface play key role.[60] In Fe_3O_4 LIBs, there exists a space charge zone formed by spin-polarized electrons at the interface between magnetic nanosized Fe particles and Li_2O, which is the surface capacitance for extra lithium storage.[60] The actual capacitance of $CoSe_2$ with orthogonal structure is higher than that of cubic system may be derived from the surface capacitance. If the magnetic nanoparticles of Co form a surface capacitance with K_2Se, then the PIBs capacity should be the same whether it is orthogonal or cubic $CoSe_2$. But in fact, the electrochemical performance of orthogonal $CoSe_2$ is better, no matter PIBs in Table S1† and SIBs in Table S2.† Therefore, for $CoSe_2$@N-rGO PIBs is different from that of Fe_3O_4 LIBs. It can be speculated that during the electrochemical cycling of $CoSe_2$@N-rGO PIBs, there may be minor remaining orthorhombic $CoSe_2$ and the product K_2Se to form surface capacitance of spin-polarized electrons.

In PIBs and SIBs, the heterojunction can be formed between two different phases, such as sodium/potassium-ion storage anode $Ni_3Se_4/CoSe_2$. For $CoSe_2$ with different phases, it is also possible to form heterojunctions in principle. The DOS profiles of orthorhombic $CoSe_2$/cubic $CoSe_2$ are shown in Fig. 6(c). On one hand, the elimination of the bandgap between 3–5 V and the overall higher total DOS, indicating that the heterointerface of orthorhombic $CoSe_2$/cubic $CoSe_2$ enhances electrical conductivity compared with single phase of $CoSe_2$. Fig. 6(f) shows that the DOS of carbon coated heterojunction is not much different from Fig. 6(d) and (e). In our experiments, since the content of cubic $CoSe_2$ is small, the probability of forming heterojunction is lower. Therefore, in the subsequent experiments, it is necessary to construct a phase that can form a relatively perfect heterojunction between orthorhombic $CoSe_2$ and cubic $CoSe_2$, which should be further improve the specific capacity of PIBs.

4. Conclusion

In summary, we successfully synthesized N-doped rGO tightly encapsulated $CoSe_2$ with mixed phases by one-step hydrothermal method. The experimental and DFT results show that the capacity of $CoSe_2$@N-rGO is 559.3 mA h g^{-1} during the first charge/discharge at a current density of 0.05 A g^{-1}, and importantly, the capacity remains stable at 421 mA h g^{-1} after 100 cycles at a high current density of 0.2 A g^{-1}. The excellent rate performance and long cycle life of the $CoSe_2$@N-rGO electrode provide beneficial help for the development of novel PIBs anode materials.

Author contributions

Hui Zheng, Han-Shu Xu, Huimin Liu, Lianwei Wei, Shusheng Wu, Jin Li, and Yuhu Huang made the samples, performed the measurements and analyzed the data with help from Han-Shu Xu and Kaibin Tang. Jiaping Hu performed the DFT calculations. Hui Zheng, Han-Shu Xu, and Kaibin Tang wrote the paper with input from all other co-authors.

Conflicts of interest

There are no conflicts to declare.

Acknowledgements

We sincerely appreciate the fund support of the National Key R&D Program of China (2021YFB4001401) and the National Natural Science Foundation of China (21671182).

References

1 J. Zhao, Y. Zhang, Y. Wang, H. Li and Y. Peng, The application of nanostructured transition metal sulfides as anodes for lithium ion batteries, *J. Energy Chem.*, 2018, **27**, 1536–1554.
2 F. Arshad, J. Lin, N. Manurkar, E. Fan, A. Ahmad, M.-u.-N. Tariq, F. Wu, R. Chen and L. Li, Life Cycle Assessment of Lithium-ion Batteries: A Critical Review, *Resour., Conserv. Recycl.*, 2022, **180**, 106104.
3 J. Xie and Y. C. Lu, A retrospective on lithium-ion batteries, *Nat. Commun.*, 2020, **11**, 2499.
4 S. Xiao, X. Li, T. Li, Y. Xiang and J. S. Chen, Practical strategies for enhanced performance of anode materials in Na^+/K^+-ion batteries, *J. Mater. Chem. A*, 2021, **9**, 7317–7335.
5 T. L. Kulova, V. N. Fateev, E. A. Seregina and A. S. Grigoriev, A Brief Review of Post-Lithium-Ion Batteries, *Int. J. Electrochem. Sci.*, 2020, **15**, 7242–7259.
6 Y. Lu, A. P. V. K. Saroja, R. Wei and Y. Xu, Engineering metal selenides for sodium-and potassium-ion batteries, *Cell Rep. Phys. Sci.*, 2021, **2**, 100555.
7 X. Min, J. Xiao, M. Fang, W. Wang, Y. Zhao, Y. Liu, A. M. Abdelkader, K. Xi, R. V. Kumar and Z. Huang, Potassium-ion batteries: outlook on present and future technologies, *Energy Environ. Sci.*, 2021, **14**, 2186–2243.
8 P. Li, H. Kim, K. H. Kim, J. Kim, H. G. Jung and Y. K. Sun, State-of-the-art anodes of potassium-ion batteries: synthesis, chemistry, and applications, *Chem. Sci.*, 2021, **12**, 7623–7655.
9 W. Zhang, J. Yin, W. Wang, Z. Bayhan and H. N. Alshareef, Status of rechargeable potassium batteries, *Nano Energy*, 2021, **83**, 105792.
10 Y. Dong, C. Yan, H. Zhao and Y. Lei, Recent Advances in 2D Heterostructures as Advanced Electrode Materials for Potassium-Ion Batteries, *Small Struct.*, 2022, **3**, 2100221.
11 P. Du, L. Cao, B. Zhang, C. Wang, Z. Xiao, J. Zhang, D. Wang and X. Ou, Recent progress on heterostructure materials for next-generation sodium/potassium ion batteries, *Renewable Sustainable Energy Rev.*, 2021, **151**, 111640.
12 M. M. Rahman, I. Sultana, Y. Fan, B. Yu, T. Tao, C. Hou and Y. Chen, Strategies, design and synthesis of advanced nanostructured electrodes for rechargeable batteries, *Mater. Chem. Front.*, 2021, **5**, 5897–5931.
13 Z. Jian, W. Luo and X. Ji, Carbon electrodes for K-ion batteries, *J. Am. Chem. Soc.*, 2015, **137**, 11566–11569.
14 P. Xiong, J. Zhu, L. Zhang and X. Wang, Recent advances in graphene-based hybrid nanostructures for electrochemical energy storage, *Nanoscale Horiz.*, 2016, **1**, 340–374.
15 Y. An, H. Fei, G. Zeng, L. Ci, B. Xi, S. Xiong and J. Feng, Commercial expanded graphite as a low-cost, long-cycling life anode for potassium-ion batteries with conventional carbonate electrolyte, *J. Power Sources*, 2018, **378**, 66–72.
16 J. Bai, H. Wu, S. Wang, G. Zhang, C. Feng and H. Liu, Synthesis of $CoSe_2$-$SnSe_2$ nanocube-coated nitrogen-doped carbon (NC) as anode for lithium and sodium ion batteries, *Appl. Surf. Sci.*, 2019, **488**, 512–521.
17 I. Hussain, S. Sahoo, C. Lamiel, T. T. Nguyen, M. Ahmed, C. Xi, S. Iqbal, A. Ali, N. Abbas, M. S. Javed and K. Zhang, Research progress and future aspects: Metal selenides as effective electrodes, *Energy Storage Mater.*, 2022, **47**, 13–43.
18 A. Sobhani and M. Salavati-Niasari, Transition metal selenides and diselenides: Hydrothermal fabrication, investigation of morphology, particle size and and their

applications in photocatalyst, *Adv. Colloid Interface Sci.*, 2021, **287**, 102321.
19 T. Lu, S. Dong, C. Zhang, L. Zhang and G. Cui, Fabrication of transition metal selenides and their applications in energy storage, *Coord. Chem. Rev.*, 2017, **332**, 75–99.
20 J. Zhou, Y. Liu, S. Zhang, T. Zhou and Z. Guo, Metal chalcogenides for potassium storage, *InfoMat*, 2020, **2**, 437–465.
21 G. D. Park, J. S. Park, J. K. Kim and Y. C. Kang, Recent Advances in Heterostructured Anode Materials with Multiple Anions for Advanced Alkali-Ion Batteries, *Adv. Energy Mater.*, 2021, **11**, 2003058.
22 Y. Zhang, S. Wei, Z. Zhao, X. Pei, W. Zhao, J. Wang, X. Du and D. Li, Carbon-Encapsulated $Ni_3Se_4/CoSe_2$ Heterostructured Nanospheres: Sodium/Potassium-Ion Storage Anode with Prominent Electrochemical Properties, *Small*, 2022, 2107258.
23 Y. Xu, X. Liu, H. Su, S. Jiang, J. Zhang and D. Li, Hierarchical Bimetallic Selenides $CoSe_2$-$MoSe_2$/rGO for Sodium/Potassium-Ion Batteries Anode: Insights into the Intercalation and Conversion Mechanism, *Energy Environ. Mater.*, 2022, **5**, 627–636.
24 X. Ou, X. Liang, F. Zheng, P. Wu, Q. Pan, X. Xiong, C. Yang and M. Liu, *In situ* X-ray diffraction investigation of $CoSe_2$ anode for Na-ion storage: Effect of cut-off voltage on cycling stability, *Electrochim. Acta*, 2017, **258**, 1387–1396.
25 H. Guo, G. Liu, M. Wang, Y. Zhang, W. Li, K. Chen, Y. Liu, M. Yue and Y. Wang, *In Situ* Fabrication of Bone-Like $CoSe_2$ Nano-Thorn Loaded on Porous Carbon Cloth as a Flexible Electrode for Na-Ion Storage, *Chem.–Asian J.*, 2020, **15**, 1493–1499.
26 N. Yu, L. Zou, C. Li and K. Guo, *In situ* growth of binder-free hierarchical carbon coated $CoSe_2$ as a high performance lithium ion battery anode, *Appl. Surf. Sci.*, 2019, **483**, 85–90.
27 J. Geng, S. Zhang, E. H. Ang, J. Guo, Z. Jin, X. Li, Y. Cheng, H. Dong and H. Geng, Modulating the kinetics of $CoSe_2$ yolk-shell spheres *via* nitrogen doping with high pseudocapacitance toward ultra-high-rate capability and high-energy density sodium-ion half/full batteries, *Mater. Chem. Front.*, 2021, **5**, 6873–6882.
28 S. H. Yang, S. K. Park and Y. C. Kang, MOF-Derived $CoSe_2$@N-Doped Carbon Matrix Confined in Hollow Mesoporous Carbon Nanospheres as High-Performance Anodes for Potassium-Ion Batteries, *Nano-Micro Lett.*, 2021, **13**, 1–15.
29 F. Kong, J. Wang, J. Chen, S. Tao, B. Qian and H. Luo, MOF-derived ultrasmall $CoSe_2$ nanoparticles encapsulated by an N-doped carbon matrix and their superior lithium/sodium storage properties, *Chem. Commun.*, 2020, **56**, 9218–9221.
30 H. Zhou, X. Li, Y. Li, M. Zheng and H. Pang, Applications of M_xSe_y (M = Fe, Co, Ni) and Their Composites in Electrochemical Energy Storage and Conversion, *Nano-Micro Lett.*, 2019, **11**, 1–33.
31 Y. Zhao, Y. Yan and J. M. Lee, Recent progress on transition metal diselenides from formation and modification to applications, *Nanoscale*, 2022, **14**, 1075–1095.
32 H. Zhao, Y. Qi, K. Liang, J. Li, L. Zhou, J. Chen, X. Huang and Y. Ren, Interface-Driven Pseudocapacitance Endowing Sandwiched $CoSe_2$/N-Doped Carbon/TiO_2 Microcubes with Ultra-Stable Sodium Storage and Long-Term Cycling Stability, *ACS Appl. Mater. Interfaces*, 2021, **13**, 61555–61564.
33 Y. Liu, Z. Chen, H. Jia, H. Xu, M. Liu and R. Wu, Iron-Doping-Induced Phase Transformation in Dual-Carbon-Confined Cobalt Diselenide Enabling Superior Lithium Storage, *ACS Nano*, 2019, **13**, 6113–6124.
34 J. Xie, Y. Zhu, N. Zhuang, H. Lei, W. Zhu, Y. Fu, M. S. Javed, J. Li and W. Mai, Rational design of metal organic framework-derived FeS_2 hollow nanocages@reduced graphene oxide for K-ion storage, *Nanoscale*, 2018, **10**, 17092–17098.
35 Z. Zhao, C. Gao, J. Fan, P. Shi, Q. Xu and Y. Min, Dual Confinement of $CoSe_2$ Nanorods with Polyphosphazene-Derived Heteroatom-Doped Carbon and Reduced Graphene Oxide for Potassium-Ion Batteries, *ACS Omega*, 2021, **6**, 17113–17125.
36 Z. Li, L. Y. Zhang, L. Zhang, J. Huang and H. Liu, ZIF-67-derived CoSe/NC composites as anode materials for lithium-ion batteries, *Nanoscale Res. Lett.*, 2019, **14**, 1–11.
37 E. Xu, P. Li, J. Quan, H. Zhu, L. Wang, Y. Chang, Z. Sun, L. Chen, D. Yu and Y. Jiang, Dimensional Gradient Structure of $CoSe_2$@CNTs-MXene Anode Assisted by Ether for High-Capacity, Stable Sodium Storage, *Nano-Micro Lett.*, 2021, **13**, 1–14.
38 J. Yang, H. Gao, S. Men, Z. Shi, Z. Lin, X. Kang and S. Chen, $CoSe_2$ nanoparticles encapsulated by N-doped carbon framework intertwined with carbon nanotubes: high-performance dual-role anode materials for both Li- and Na-ion batteries, *Adv. Sci.*, 2018, **5**, 1800763.
39 Z. Li, H. Xue, J. Wang, Y. Tang, C.-S. Lee and S. Yang, Reduced Graphene Oxide/Marcasite-Type Cobalt Selenide Nanocrystals as an Anode for Lithium-Ion Batteries with Excellent Cyclic Performance, *ChemElectroChem*, 2015, **2**, 1682–1686.
40 Y. Xiao, P. Sun and M. Cao, Core-Shell Bimetallic Carbide Nanoparticles Confined in a Three-Dimensional N-Doped Carbon Conductive Network for Efficient Lithium Storage, *ACS Nano*, 2014, **8**, 7846–7857.
41 H. Liu, D. Su, R. Zhou, B. Sun, G. Wang and S. Z. Qiao, Highly Ordered Mesoporous MoS_2 with Expanded Spacing of the (002) Crystal Plane for Ultrafast Lithium Ion Storage, *Adv. Energy Mater.*, 2012, **2**, 970–975.
42 Z. Zhang, B. Zhang, J. Xu, M. Zhang, L. Duan, J. Shen and X. Zhou, Anchoring Carbon-Coated CoSe Nanoparticles on Hollow Carbon Nanocapsules for Efficient Potassium Storage, *ACS Appl. Energy Mater.*, 2021, **4**, 6356–6363.
43 Y. Wang, Y. Wu, L. Liu, T. Yan, G. Zeng, L. Li, J. Duan and Z. Chen, Bimetallic MOF-derived $CoSe_2$ embedded within N-doped carbon with enhanced lithium storage properties, *Solid State Ionics*, 2021, **370**, 115747.
44 N. Hussain, M. Li, B. Tian and H. Wang, Co_3Se_4 Quantum Dots as an Ultrastable Host Material for Potassium-Ion Intercalation, *Adv. Mater.*, 2021, **33**, 2102164.

45 C. Wang, B. Zhang, X. Ou, H. Xia, L. Cao, L. Ming and J. Zhang, $Co_{0.85}Se$@N-doped reduced graphene oxide hybrid polyhedron-in-polyhedron structure assembled from metal-organic framework with enhanced performance for Li-ion storage, *J. Colloid Interface Sci.*, 2020, **573**, 223–231.

46 Y. Xiao, J. Zhang, D. Su, A. Zhang, Q. Jin, L. Zhou, S. Wu, X. Wang, W. Chen and S. Fang, *In situ* growth of V-shaped $CoSe_2$ nanorods on graphene with C-Co bonding for high-rate and long-life sodium-ion batteries, *J. Alloys Compd.*, 2020, **819**, 153359.

47 C. Cui, Z. Wei, G. Zhou, W. Wei, J. Ma, L. Chen and C. Li, Quasi-reversible conversion reaction of $CoSe_2$/nitrogen-doped carbon nanofibers towards long-lifetime anode materials for sodium-ion batteries, *J. Mater. Chem. A*, 2018, **6**, 7088–7098.

48 J. Hu, B. Wang, Q. Yu, D. Zhang, Y. Zhang, Y. Li and W. A. Wang, $CoSe_2$/N-doped carbon porous nanoframe as an anode material for potassium-ion storage, *Nanotechnology*, 2020, **31**, 395403.

49 Q. Yu, B. Jiang, J. Hu, C. Y. Lao, Y. Gao, P. Li, Z. Liu, G. Suo, D. He, W. A. Wang and G. Yin, Metallic Octahedral $CoSe_2$ Threaded by N-Doped Carbon Nanotubes: A Flexible Framework for High-Performance Potassium-Ion Batteries, *Adv. Sci.*, 2018, **5**, 1800782.

50 H. Hu, J. Zhang, B. Guan and X. W. Lou, Unusual formation of CoSe@carbon nanoboxes, which have an inhomogeneous shell, for efficient lithium storage, *Angew. Chem., Int. Ed.*, 2016, **55**, 9514–9518.

51 Z. Liu, K. Han, P. Li, W. Wang, D. He, Q. Tan, L. Wang, Y. Li, M. Qin and X. Qu, Tuning Metallic $Co_{0.85}Se$ Quantum Dots/Carbon Hollow Polyhedrons with Tertiary Hierarchical Structure for High-Performance Potassium Ion Batteries, *Nano-Micro Lett.*, 2019, **11**, 1–14.

52 W. Wang, J. Zhou, Z. Wang, L. Zhao, P. Li, Y. Yang, C. Yang, H. Huang and S. Guo, Short-Range Order in Mesoporous Carbon Boosts Potassium-Ion Battery Performance, *Adv. Energy Mater.*, 2018, **8**, 1701648.

53 H. Huang, R. Xu, Y. Feng, S. Zeng, Y. Jiang, H. Wang, W. Luo and Y. Yu, Sodium/potassium-ion batteries: boosting the rate capability and cycle life by combining morphology, defect and structure engineering, *Adv. Mater.*, 2020, **32**, 1904320.

54 Y. Liu, Q. Deng, Y. Li, Y. Li, W. Zhong, J. Hu, X. Ji, C. Yang, Z. Lin and K. Huang, CoSe@ N-doped carbon nanotubes as a potassium-ion battery anode with high initial coulombic efficiency and superior capacity retention, *ACS Nano*, 2021, **15**, 1121–1132.

55 V. Augustyn, P. Simon and B. Dunn, Pseudocapacitive oxide materials for high-rate electrochemical energy storage, *Energy Environ. Sci.*, 2014, **7**, 1597–1614.

56 T. Brezesinski, J. Wang, J. Polleux, B. Dunn and S. H. Tolbert, Templated nanocrystal-based porous TiO_2 films for next-generation electrochemical capacitors, *J. Am. Chem. Soc.*, 2009, **131**, 1802–1809.

57 P. Lou, Z. Cui, Z. Jia, J. Sun, Y. Tan and X. Guo, Monodispersed carbon-coated cubic NiP_2 nanoparticles anchored on carbon nanotubes as ultra-long-life anodes for reversible lithium storage, *ACS Nano*, 2017, **11**, 3705–3715.

58 Q. Yu, B. Jiang, J. Hu, C. Y. Lao, Y. Gao, P. Li, Z. Liu, G. Suo, D. He and W. Wang, Metallic octahedral $CoSe_2$ threaded by N-doped carbon nanotubes: a flexible framework for high-performance potassium-ion batteries, *Adv. Sci.*, 2018, **5**, 1800782.

59 A. Teruya, F. Suzuki, D. Aoki, F. Honda, A. Nakamura, M. Nakashima, Y. Amako, H. Harima, K. Uchima, and M. Hedo, in Fermi Surface and Magnetic Properties in Ferromagnet CoS_2 and Paramagnet $CoSe_2$ with the Pyrite-type Cubic Structure, *Journal of Physics: Conference Series*, IOP Publishing, 2017; p. 012001.

60 Q. Li, H. Li, Q. Xia, Z. Hu, Y. Zhu, S. Yan, C. Ge, Q. Zhang, X. Wang and X. Shang, Extra storage capacity in transition metal oxide lithium-ion batteries revealed by *in situ* magnetometry, *Nat. Mater.*, 2021, **20**, 76–83.